

Strain-tunable orbital, spin-orbit, and optical properties of monolayer transition-metal dichalcogenides

Klaus Zollner,^{1,*} Paulo E. Faria Junior,¹ and Jaroslav Fabian¹

¹*Institute for Theoretical Physics, University of Regensburg, 93040 Regensburg, Germany*

(Dated: November 20, 2019)

When considering transition-metal dichalcogenides (TMDCs) in van der Waals (vdW) heterostructures for periodic *ab-initio* calculations, usually, lattice mismatch is present, and the TMDC needs to be strained. In this study we provide a systematic assessment of biaxial strain effects on the orbital, spin-orbit, and optical properties of the monolayer TMDCs using *ab-initio* calculations. We complement our analysis with a minimal tight-binding Hamiltonian that captures the low-energy bands of the TMDCs around K and K' valleys. We find characteristic trends of the orbital and spin-orbit parameters as a function of the biaxial strain. Specifically, the orbital gap decreases linearly, while the valence (conduction) band spin splitting increases (decreases) nonlinearly in magnitude when the lattice constant increases. Furthermore, employing the Bethe-Salpeter equation and the extracted parameters, we show the evolution of several exciton peaks, with biaxial strain, on different dielectric surroundings, which are particularly useful for interpreting experiments studying strain-tunable optical spectra of TMDCs.

Keywords: TMDC, straintronics, excitons

I. INTRODUCTION

A vastly evolving field of condensed matter physics is that of two-dimensional (2D) van der Waals (vdW) materials and their hybrids. The available material repertoire covers semiconductors [1–5] (MoS₂, WSe₂), ferromagnets [6–21] (CrI₃, CrGeTe₃), superconductors [22–24] (NbSe₂), and topological insulators [25] (WTe₂), which offer unforeseen potential for electronics and spintronics [26, 27]. For example, monolayer transition-metal dichalcogenides (TMDCs) are direct band gap semiconductors with remarkable physical properties [1–5, 28–31], specially in the realm of optoelectronics [32], optospintronics [33–35], and valleytronics [36–38]. Currently, TMDCs, being stable in air, are a favorite platform for optical experiments including optical spin injection due to helicity-selective optical excitations [39].

The ability to control and modify the electronic, spin, and optical properties of 2D materials is extremely valuable for investigating novel physical phenomena, as well as a potential knob for device applications. One possibility to do so in TMDCs is by deforming the crystal lattice via strain engineering [40–52]. Recent experiments have shown that strain modulation is very effective and can lead to changes in the optical transition energies by hundreds of meV with just a few percent of applied strain [40, 41, 44–47]. Even more interesting is that this strain modulation is completely reversible [44, 45]. As a general trend observed in the experimental studies, biaxial strain induces a significantly stronger modulation when compared to uniaxial strain, a fact also supported by *ab-initio* calculations [53, 54]. Furthermore, by strain engineering it is possible to localize excitons in specific

regions, which is a viable approach to obtain spatially and spectrally isolated quantum emitters based on 2D materials [51, 55–58].

Strain also plays an important role when TMDCs are stacked on or sandwiched by other 2D materials creating vdW heterostructures [59, 60]. An example of interesting physics present in vdW heterostructures are the proximity effects [61]. Typical examples involving TMDCs are: spin-orbit coupling (SOC) induced in graphene by TMDCs [33, 62] and proximity exchange induced in the TMDC due to magnetic substrates [38, 63–65].

Strain effects are extremely important from a theoretical point of view: by creating vdW heterostructures that fulfill the periodic boundary conditions of first-principles calculations, it is often necessary to adjust the lattice parameters of the materials involved, therefore leading to strained crystals. Certainly, the strain — which is biaxial in first-principles calculations — will modify the electronic structure of the TMDC and therefore a systematic analysis of its behavior can provide valuable insight not only from an experimental point of view but also to aid in the design of novel heterostructures.

In this paper, we study the effect of biaxial strain on the orbital, spin-orbit, and optical properties of pristine monolayer TMDCs. We find that by tuning the lattice constant, the orbital band gap, and the spin splittings of the valence and conduction bands drastically change. Specifically, the orbital gap decreases linearly, while the valence (conduction) band spin splitting increases (decreases) nonlinearly in magnitude, when the lattice constant increases. The observed behavior is universal for all studied TMDCs (MoS₂, MoSe₂, WS₂, WSe₂). In addition, we show that spin splittings of the bands result from an interplay of the atomic SOC values of the transition-metal and chalcogen atoms. Finally, we analyze the direct-indirect transition energies and by employing the Bethe-Salpeter equation we calculate the op-

* klaus.zollner@physik.uni-regensburg.de

tical absorption spectra of the biaxially strained TMDC monolayers. We show the evolution of several exciton peaks and their energy differences as a function of strain, assuming different dielectric surroundings. We also extracted the gauge factors — the rates at which the exciton peak energies shift due to strain — which are relevant for comparison to experiments.

II. MODEL HAMILTONIAN

In the manuscript, we deal with TMDC monolayers. Therefore we need a Hamiltonian that describes the low energy bands of bare TMDCs around the K and K' valleys, including spin-valley locking. In Fig. 1 we show the orbital decomposed band structure of MoS₂ without inclusion of SOC, as a representative example of a TMDC with general structure MX₂ (M for the transition metal atom, X for the chalcogen atom). The wave

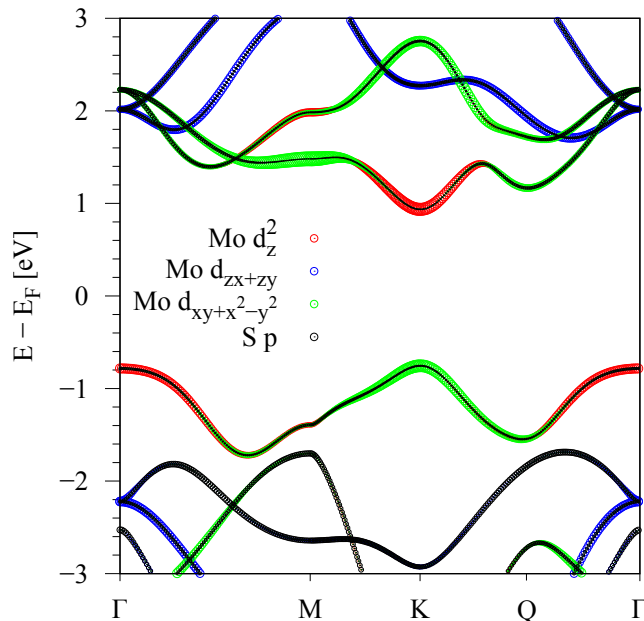


FIG. 1. (Color online) Calculated orbital decomposed band structure of MoS₂, as a representative example of a TMDC. SOC is not included and the different colors correspond to different orbitals or atoms.

functions we use for the Hamiltonian are $|\Psi_{CB}\rangle = |d_{z^2}\rangle$ and $|\Psi_{VB}^\tau\rangle = \frac{1}{\sqrt{2}}(|d_{x^2-y^2}\rangle + i\tau|d_{xy}\rangle)$, corresponding to the conduction band (CB) and the valence band (VB) at K and K', since the band edges are formed by different *d*-orbitals from the transition metal, see Fig. 1, in agreement with literature [1]. The model Hamiltonian to describe the band structure (including SOC) of the

TMDC close to K ($\tau = 1$) and K' ($\tau = -1$) is

$$\mathcal{H} = \mathcal{H}_0 + \mathcal{H}_\Delta + \mathcal{H}_{\text{soc}}, \quad (1)$$

$$\mathcal{H}_0 = \hbar v_F s_0 \otimes (\tau \sigma_x k_x + \sigma_y k_y), \quad (2)$$

$$\mathcal{H}_\Delta = \frac{\Delta}{2} s_0 \otimes \sigma_z, \quad (3)$$

$$\mathcal{H}_{\text{soc}} = \tau s_z \otimes (\lambda_c \sigma_+ + \lambda_v \sigma_-). \quad (4)$$

Here, v_F is the Fermi velocity and the Cartesian components k_x and k_y of the electron wave vector are measured from K (K'). The pseudospin Pauli matrices are σ_i acting on the (CB,VB) subspace and spin Pauli matrices are s_i acting on the (\uparrow, \downarrow) subspace, with $i = \{0, x, y, z\}$. For shorter notation we introduce $\sigma_\pm = \frac{1}{2}(\sigma_0 \pm \sigma_z)$. TMDCs are semiconductors, and thus \mathcal{H}_Δ introduces a gap, represented by parameter Δ , in the band structure such that $\mathcal{H}_0 + \mathcal{H}_\Delta$ describes a gapped spectrum with spin-degenerate parabolic CB and VB. In addition the bands are spin-split due to SOC which is captured by the term \mathcal{H}_{soc} with the parameters λ_c and λ_v describing the spin splitting of the CB and VB. The Hamiltonian $\mathcal{H}_0 + \mathcal{H}_\Delta + \mathcal{H}_{\text{soc}}$ is already suitable to describe the spectrum of bare TMDCs around the band edges at K and K'. The four basis states are $|\Psi_{CB, \uparrow}\rangle$, $|\Psi_{VB, \uparrow}^\tau\rangle$, $|\Psi_{CB, \downarrow}\rangle$, and $|\Psi_{VB, \downarrow}^\tau\rangle$. From now on, we consider only first-principles results, where SOC is included.

III. GEOMETRY, BAND STRUCTURE, AND FITTED RESULTS

To study proximity effects in TMDCs, one has to interface them with other materials, for example CrI₃ to get proximity exchange [63]. In these heterostructures, usually lattice mismatch between the constituents is present, and we have to find a common unit cell for them, to be applicable to periodic DFT calculations. The usual approach is to create supercells of the individual materials, such that they can form a common unit cell, and strain is minimized. Therefore, we introduce biaxial strain on the TMDC lattice, up to a reasonable limit, in heterostructure calculations. An important question is, whether the biaxial strain, will influence the *intrinsic* properties, such as orbital gap and spin-orbit splittings, of the TMDC. Therefore, we calculate the band structures of the monolayer TMDCs in a 1×1 unit cell for different lattice constants, corresponding to biaxial strain with a maximum of $\pm 3\%$.

The electronic structure calculations and structural relaxation of our geometries are performed with density functional theory (DFT) [66] using QUANTUM ESPRESSO [67]. Self-consistent calculations are performed with the *k*-point sampling of $30 \times 30 \times 1$ for bare TMDC monolayers. We use an energy cutoff for charge density of 560 Ry, and the kinetic energy cutoff for wavefunctions is 70 Ry for the scalar relativistic pseudopotential with the projector augmented wave method [68] with the Perdew-Burke-Ernzerhof (PBE) exchange correlation

functional [69]. When SOC is included, the fully relativistic versions of the pseudopotentials are used. In order to simulate quasi-2D systems, a vacuum of at least 16 Å is used to avoid interactions between periodic images in our slab geometries. Structural relaxations of the monolayers, are performed with a quasi-Newton algorithm based on the trust radius procedure, until all components of all forces are reduced below 10^{-4} [Ry/ a_0], where a_0 is the Bohr radius.

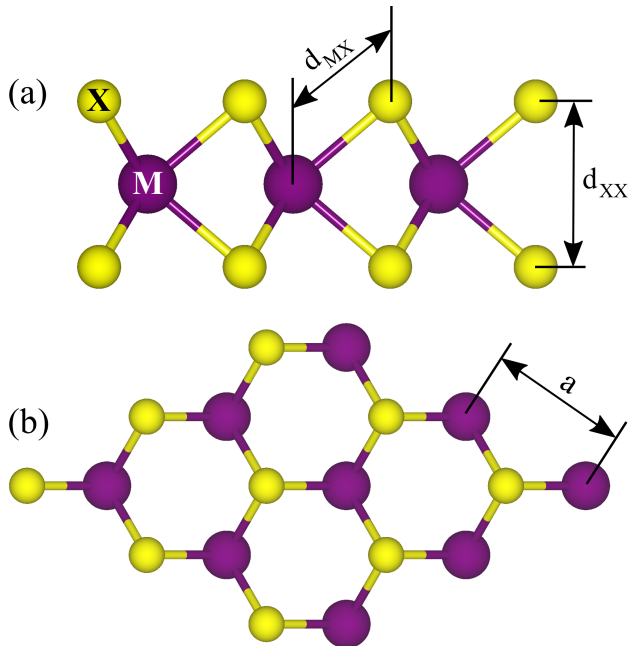


FIG. 2. (Color online) Geometry of a TMDC monolayer with general structure MX_2 , where M is the transition metal (Mo, W) and X is the chalcogen atom (S, Se). (a) Side and (b) top view of the geometry, with labels for the lattice constant a , distance d_{MX} (between the transition metal and the chalcogen atom), and d_{XX} (between the two chalcogen atoms).

In Fig. 2 we show the geometry of a TMDC monolayer with general structure MX_2 , where M is the transition metal (Mo, W) and X is the chalcogen atom (S, Se). The distance between two chalcogen atoms is d_{XX} , the distance between the transition metal and the chalcogen atom is d_{MX} , and the distance between two transition metal atoms is the lattice constant a . We consider a series of lattice constants, close to the experimental and theoretically predicted values of each TMDC, as summarized in Table I.

The calculated band structure of MoS_2 including SOC is shown in Fig. 3 as a representative example for all considered TMDCs. In agreement with previous calculations [1, 2, 73, 74], we observe the spin valley coupling at K and K' point. We are able to fit the Hamiltonian, $\mathcal{H}_0 + \mathcal{H}_\Delta + \mathcal{H}_{\text{soc}}$, to the low energy bands of the TMDC at K and K' valley and obtain a very good agreement with the calculated band structure, as can be seen in Figs. 3(b,c). The fit parameters for the different TMDCs are

TABLE I. Overview of the lattice parameters for all TMDCs, as well as fit parameters of the Hamiltonian $\mathcal{H}_0 + \mathcal{H}_\Delta + \mathcal{H}_{\text{soc}}$. The monolayer calculated lattice constant a (calc.), distances d_{XX} , and d_{MX} , as defined in Fig 2. The orbital gap parameter Δ , the Fermi velocity v_{F} and the SOC parameters λ_{c} and λ_{v} . The experimental lattice constants a (exp.) [70–72] of the bulk systems are given for comparison.

| | MoS ₂ | WS ₂ | MoSe ₂ | WSe ₂ |
|---|------------------|-----------------|-------------------|------------------|
| a (exp.) [Å] | 3.15 | 3.153 | 3.288 | 3.282 |
| a (calc.) [Å] | 3.185 | 3.18 | 3.319 | 3.319 |
| d_{MX} (calc.) [Å] | 2.417 | 2.417 | 2.547 | 2.550 |
| d_{XX} (calc.) [Å] | 3.138 | 3.145 | 3.357 | 3.364 |
| Δ [eV] | 1.687 | 1.812 | 1.461 | 1.525 |
| v_{F} [$10^5 \frac{\text{m}}{\text{s}}$] | 5.338 | 6.735 | 4.597 | 5.948 |
| λ_{c} [meV] | -1.41 | 15.72 | -10.45 | 19.86 |
| λ_{v} [meV] | 74.6 | 213.46 | 93.25 | 233.07 |

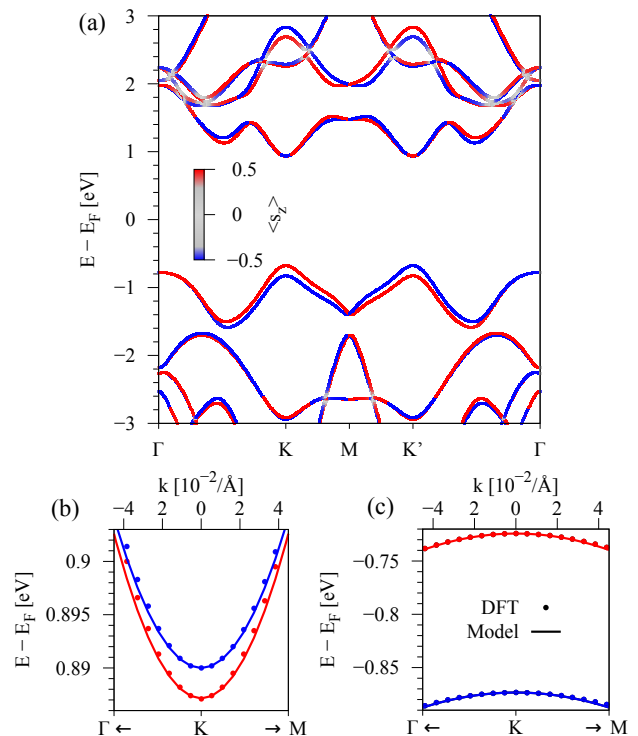


FIG. 3. (Color online) (a) Calculated band structure of MoS_2 including SOC. The color corresponds to the s_z expectation value. (b,c) Calculated low energy CB and VB around the K point (symbols) with a fit to the model Hamiltonian (solid line).

summarized in Table I, considering the equilibrium lattice constants obtained from first-principles lattice relaxation.

In order to analyze the dependence on the lattice constant, i. e., biaxial strain, we allow the chalcogen atoms to relax in their z position, for every considered lattice constant. Therefore, we do not change the symmetry,

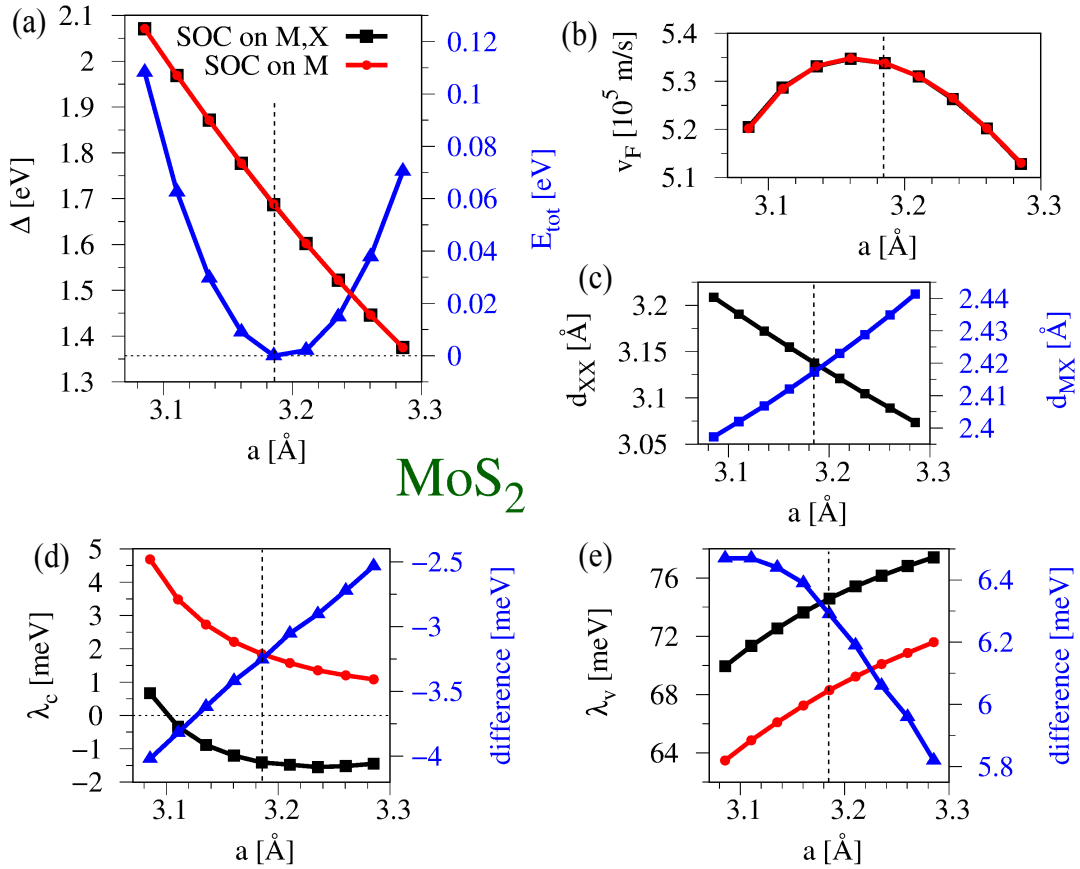


FIG. 4. (Color online) Summary of the fit parameters for MoS₂ as a function of the lattice constant. (a) The gap parameter Δ and the total energy E_{tot} . The black data (SOC on M,X) correspond to calculations where SOC is included for both atoms M and X, while for the red data (SOC on M), we turned off SOC on the X atoms. Dashed vertical lines indicate the equilibrium lattice constant. (b) The Fermi velocity v_F . (c) The distances d_{XX} and d_{MX} . (d,e) The SOC parameters λ_c and λ_v . The difference (blue curve) is between the black and the red curve.

but naturally the distances d_{XX} and d_{MX} will change, as we apply biaxial strain. We then calculate the low energy band structure around the K and K' valleys and fit the model Hamiltonian $\mathcal{H}_0 + \mathcal{H}_\Delta + \mathcal{H}_{\text{SOC}}$, for a series of lattice constants. Due to time-reversal symmetry, it is enough to fit the Hamiltonian around the K point, taking into account the spin expectation values of the bands in order to find the correct signs of λ_c and λ_v . The three parameters Δ , λ_c , and λ_v are fitted at the K point, where we have four DFT-energies and three energy differences. The remaining parameter v_F is fitted around the K point, to capture the curvature of the bands. The fitted parameters are thus free from correlations. In Fig. 4 we show the fit parameters obtained for MoS₂ as function of the lattice constant. We find that the total energy E_{tot} is minimized for the DFT predicted lattice constant [1], which slightly deviate from the experimentally determined one for a bulk TMDC, also listed in Table I.

As we vary the lattice constant from smaller to larger values the distance between two chalcogen atoms d_{XX} is getting smaller, while the distance between the transition metal atom and the chalcogen atom d_{MX} is getting larger,

see Fig. 4(c). The parameter Δ , describing the orbital gap at K and K' valley, decreases as we increase the lattice constant in agreement with literature [48, 54, 75–78]. Keeping the orbital decomposed band structure (Fig. 1) in mind, the lattice constant influences all atomic distances, the overlap of p and d -orbitals, and matrix elements in a tight-binding model perspective [79, 80]. Consequently, the energy of a given band at a certain k -point changes with the atomic distances. For example, the CB (VB) edge at the K (Γ) point is formed by d_{z^2} -orbitals and shifts down (up) in energy with increasing lattice constant, see animations in the Supplemental Material [81].

Note that for MoS₂ and strains of about -1% ($+1\%$), when we have a smaller (larger) lattice constant, the band gap becomes indirect [54, 76, 77] and is at $K \rightarrow Q$ ($\Gamma \rightarrow K$), where Q is the CB side valley along the K- Γ line, see Fig. 1. For the other TMDCs, the situation is similar, but for different strain amplitudes. Tuning the gap with uniaxial or biaxial strain consequently modifies the optical properties, such as the photoluminescence spectrum, exciton-phonon coupling and circular dichroism [46, 82–

84]. It has also been shown that strain applied to MoS₂-based photodetectors can control the response time of the devices [49]. We address the effects of strain in the direct-indirect optical transitions in Sec. IV A and the role of excitonic effects in the direct gap regime in Sec. IV B.

The Fermi velocity, v_F , reflecting the effective mass, does not change drastically as we vary the lattice constant, but still we see some characteristic nonlinear behavior, see Fig. 4(b). The reason is that $v_F \propto at$ [39], given by the effective hopping integral t between d_{z^2} and $d_{xy+x^2-y^2}$ orbitals, mediated by chalcogen p orbitals, is influenced by atomic distances d_{XX} and d_{MX} . The most interesting are the SOC parameters λ_c and λ_v , see Figs. 4(d,e). Because we have two different atomic species in the unit cell, we consider the influence of the individual atoms, M and X, on the SOC parameters, which represent the spin-splittings of the CB and VB. For that we calculate the band structure once with SOC on both atom species and once artificially turning off SOC on the chalcogen atom, by using a non-relativistic pseudopotential for it. This allows us to resolve the contributions from the M and X atom to the SOC parameters individually. The difference (blue curve) reflects the contribution from the chalcogen atoms to the splittings, see Figs. 4(d,e).

We find that the parameter λ_c decreases, while the parameter λ_v increases with increasing lattice constant. Both parameters depend in a nonlinear fashion on the biaxial strain. At a certain lattice constant, the CB splitting in MoS₂ can even make a transition through zero, reordering the two spin-split bands in Fig. 3(b). In addition, the differences (blue curve) in λ_c and λ_v decrease in magnitude, as we increase the lattice constant. This we can understand from the fact, that the spin-splittings of the CB and VB result from an interplay of the atomic SOC values of the transition-metal and chalcogen atoms, as derived from perturbation theory in Ref. [74]. We confirm that the chalcogen atom has a negative contribution to the CB splitting and a positive contribution to the VB splitting, while the transition metal atom gives positive contributions to both splittings, in agreement with Ref. [74]. In Fig. 4 we explicitly show, how the spin splittings depend on the lattice constant and how the different atom types contribute to it for the case of MoS₂. What is still missing so far, is a microscopic orbital-based description of how the spin splittings depend on the lattice constant and respective distances, as for example derived for graphene [85].

In a fashion similar to Fig. 4 we calculate the same dependence on the lattice constant for other TMDCs, see Supplemental Material [81]. For all of them, we can observe similar characteristic trends of the parameters, varying as function of the lattice constant. The fitted parameters as a function of the lattice constant are summarized in Table II for all TMDCs. An interesting observation is that the CB SOC parameter λ_c for Mo-based systems is opposite in sign compared to W-based materials, as already pointed out in earlier works [1, 73, 74].

In the Supplemental Material [81] we provide anima-

tions that explicitly show the evolution of the TMDC band structures as function of biaxial strain. Additionally, we compare the results for all TMDCs obtained from two different exchange correlation functionals, namely PBE [69] and PBEsol [86]. In the case of PBEsol, which improves equilibrium properties, the total energy is minimized for the experimental lattice constant. However, the overall magnitudes and trends of the parameters as function of the lattice constant, are barely different. We conclude that the PBEsol functional should hardly influence the following results on exciton energy levels and gauge factors, and results can be compared to experiment, when regarding them relative to 0% strain (equilibrium lattice constant).

IV. STRAIN TUNABLE OPTICAL TRANSITIONS

A. Direct and indirect band gap regimes

In the previous section we analyzed the strain effects in the band structure of MoS₂ and found that different strain regimes induce a direct to indirect band gap transition. This feature is also present in the other TMDCs we investigated (see Supplemental Material [81]). In order to obtain a deeper insight into this direct to indirect band gap switching, in this section we discuss the strain dependence of the single-particle optical transitions for all the TMDCs. We focus on the mostly affected optical transitions, depicted in Fig. 5(a) for MoS₂. The evolution of these transitions with respect to applied strain is shown in Fig. 5(b-e) for MoS₂, MoSe₂, WS₂ and WSe₂, respectively. The overall trend is similar for all TMDCs: negative strain induces indirect band gap for the K_v-K_c transition while positive strain values cause the Γ_v-K_c transition to have the smallest energy. For MoSe₂ and WSe₂ the amount of positive strain required to reach the Γ_v-K_c indirect band gap regime would be larger than the region we investigated here. Additionally, K_v-Q_c transitions show a positive slope while K_v-K_c and Γ_v-K_c show a negative slope. Although a proper comparison to uniaxial strain results may seem unfair due to the different lattice symmetries, it is still worth mentioning that Γ_v-K_c transitions have a steeper dependence than the K_v-K_c transitions, as observed experimentally for MoS₂ [41] and WS₂ [52], for instance. Furthermore, theoretical studies based on first-principles calculations have shown such dependencies not only due to uniaxial strain but also in the biaxial strain case [53, 76].

One important figure of merit to analyze the strain dependence is the so called gauge factor of the transition energies, i. e., the rate of energy shift due to the applied strain, typically given in meV/%. In Table III, we quantify the gauge factors for the different transition energies shown in Figs. 5(b-e). Although these energy transitions do not behave completely linear under strain, we assumed for simplicity a linear behavior throughout the whole

TABLE II. Fit parameters of the model Hamiltonian Eq. (1) for all four TMDCs and different values of biaxial strain. The lattice parameter a is given in Å, Δ is given in eV, v_F is given in 10^5 m/s and λ_c , λ_v are given in meV.

| MoS ₂ | | | | | MoSe ₂ | | | | |
|------------------|----------|-------|-------------|-------------|-------------------|----------|-------|-------------|-------------|
| a | Δ | v_F | λ_c | λ_v | a | Δ | v_F | λ_c | λ_v |
| 3.0854 | 2.071 | 5.205 | 0.666 | 69.95 | 3.219 | 1.779 | 4.429 | -9.120 | 89.10 |
| 3.1104 | 1.969 | 5.287 | -0.336 | 71.34 | 3.244 | 1.696 | 4.507 | -10.22 | 90.39 |
| 3.1354 | 1.871 | 5.331 | -0.887 | 72.54 | 3.269 | 1.615 | 4.560 | -10.59 | 91.54 |
| 3.1604 | 1.777 | 5.347 | -1.207 | 73.64 | 3.294 | 1.536 | 4.587 | -10.64 | 92.50 |
| 3.1854 | 1.687 | 5.338 | -1.410 | 74.60 | 3.319 | 1.461 | 4.597 | -10.45 | 93.25 |
| 3.2104 | 1.602 | 5.310 | -1.479 | 75.43 | 3.344 | 1.389 | 4.589 | -10.15 | 93.95 |
| 3.2354 | 1.522 | 5.263 | -1.550 | 76.16 | 3.369 | 1.320 | 4.564 | -9.760 | 94.42 |
| 3.2604 | 1.446 | 5.202 | -1.518 | 76.82 | 3.394 | 1.255 | 4.526 | -9.309 | 94.78 |
| 3.2854 | 1.375 | 5.128 | -1.450 | 77.42 | 3.419 | 1.194 | 4.480 | -8.780 | 94.98 |
| WS ₂ | | | | | WSe ₂ | | | | |
| a | Δ | v_F | λ_c | λ_v | a | Δ | v_F | λ_c | λ_v |
| 3.080 | 2.274 | 6.752 | 43.08 | 191.46 | 3.219 | 1.917 | 5.964 | 51.18 | 212.16 |
| 3.105 | 2.153 | 6.815 | 31.80 | 197.68 | 3.244 | 1.816 | 6.011 | 38.40 | 218.12 |
| 3.130 | 2.035 | 6.820 | 24.40 | 203.40 | 3.269 | 1.716 | 6.019 | 29.87 | 223.60 |
| 3.155 | 1.921 | 6.795 | 19.35 | 208.64 | 3.294 | 1.619 | 5.995 | 24.00 | 228.56 |
| 3.180 | 1.812 | 6.735 | 15.72 | 213.46 | 3.319 | 1.525 | 5.948 | 19.86 | 233.07 |
| 3.205 | 1.710 | 6.655 | 13.07 | 217.83 | 3.344 | 1.437 | 5.881 | 16.85 | 237.10 |
| 3.230 | 1.614 | 6.542 | 11.11 | 221.81 | 3.369 | 1.353 | 5.798 | 14.63 | 240.72 |
| 3.255 | 1.526 | 6.437 | 9.62 | 225.37 | 3.394 | 1.276 | 5.702 | 13.02 | 243.86 |
| 3.280 | 1.443 | 6.311 | 8.46 | 228.57 | 3.419 | 1.203 | 5.596 | 11.81 | 246.58 |

strain range we considered. We found that the strength of gauge factors for the indirect Γ_v - K_c transitions is nearly twice as large as the direct K_v - K_c transitions. On the other hand, the strength of the gauge factors of the indirect K_v - Q_c transitions are nearly 2 (4) times smaller than the direct K_v - K_c transitions for Mo(W)-based TMDCs. Such large differences in the gauge factors provide important information to identify the evolution of the optical spectra under applied strain.

TABLE III. Gauge factors (in meV/%) for the single-particle transitions presented in Fig. 5, extracted by linear extrapolation within the whole considered strain region.

| | MoS ₂ | MoSe ₂ | WS ₂ | WSe ₂ |
|--------------------|------------------|-------------------|-----------------|------------------|
| K_v - K_c | -112.3 | -98.2 | -133.5 | -118.8 |
| Γ_v - K_c | -239.9 | -210.2 | -254.0 | -213.4 |
| K_v - Q_c | 44.3 | 45.7 | 37.0 | 32.8 |

B. Excitonic effects in the direct band gap regime

For moderate applied strain the direct band gap at the K point remains the fundamental transition energy. In this section we investigate the role of excitonic ef-

fects to such direct transitions under the applied biaxial strain. In a simple picture, an exciton is a quasi-particle created due to the electrostatic Coulomb interaction between electrons and holes [87, 88]. Because of the weak screening of 2D materials, excitons have large binding energies and, therefore, excitonic effects dominate the optical spectra [28, 29, 31, 89]. Starting from the effective Hamiltonian given in Eq. (1) and fitted parameters given in Table II, we compute the excitonic spectra of the strained monolayer TMDCs for different bright excitonic states (the s-like excitons) that can be directly probed in experiments. We use the effective Bethe-Salpeter equation (BSE) [63, 90–94] with the electron-hole interaction mediated by the Rytova-Keldysh potential [95–98]. The screening lengths of the TMDCs are taken from the study of Berkelbach *et al.* [98]. The BSE is solved on a 2D k -grid from -0.5 to 0.5 Å⁻¹ in the k_x and k_y directions with total discretization of 101×101 points (leading to a spacing of $\Delta k = 10^{-2}$ Å⁻¹). To improve convergence, the Coulomb potential is averaged around each k -point in a square region of $-\Delta k/2$ to $\Delta k/2$ discretized with 101×101 points [63, 91].

We focus on two different exciton types: the so-called A and B excitons. In Mo(W)-based TMDCs, the A excitons are formed by the first VB and first (second) CB while B excitons are formed by the second VB and sec-

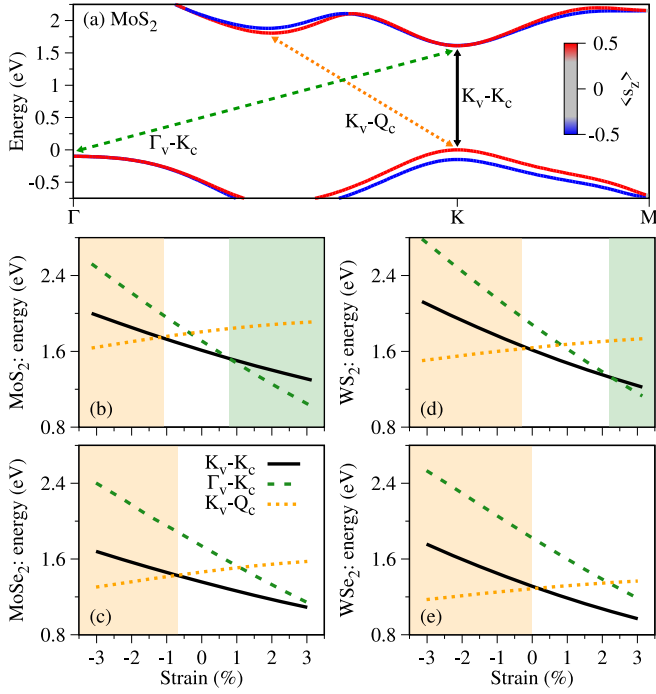


FIG. 5. (Color online) (a) Band structure of MoS_2 at zero strain highlighting the important optical transitions mostly affected by strain. The transitions are identified by the reciprocal space point (K, Q, Γ) and by the energy band (subindices v and c stand for the valence and conduction bands, respectively). Evolution of the transition energies depicted in (a) as a function of strain for (b) MoS_2 , (c) MoSe_2 , (d) WS_2 and (e) WSe_2 . The shaded regions indicate indirect band gap regimes (K-Q for negative strain and Γ -K for positive strain).

ond (first) CB, sketched in Figs. 6(a-b). In Figs. 6(c-f) we show the behavior of the total energy of A and B excitons as a function of the applied biaxial strain in two different dielectric environments: bare (effective dielectric constant of $\epsilon = 1.0$) and hexagonal boron nitride (hBN) encapsulated TMDCs (effective dielectric constant of $\epsilon = 4.5$ [99]). The subindices 1s and 2s indicate the first and second s-like exciton states, respectively. Despite the nonlinear behavior of λ_c , λ_v and ν_f seen in Fig. 4, the A excitons evolve in quite a linear fashion with the same qualitative behavior for all TMDCs. On the other hand, the B excitons show a different behavior for Mo and W-based TMDCs as function of strain. For the bare case, in Mo-based TMDCs the B exciton would be the second visible absorption peak while in W-based TMDCs additional peaks of the A excitons would be visible at energies lower than the peaks of the B excitons. Once we change the dielectric environment from bare to hBN-encapsulated, the ordering of the excitonic peaks changes in MoS_2 and MoSe_2 ; that is, the B exciton is no longer the second visible peak. Nevertheless, the same qualitative behavior as function of the biaxial strain holds, as discussed for the bare TMDCs case.

In Table IV, we present the gauge factors for the ex-

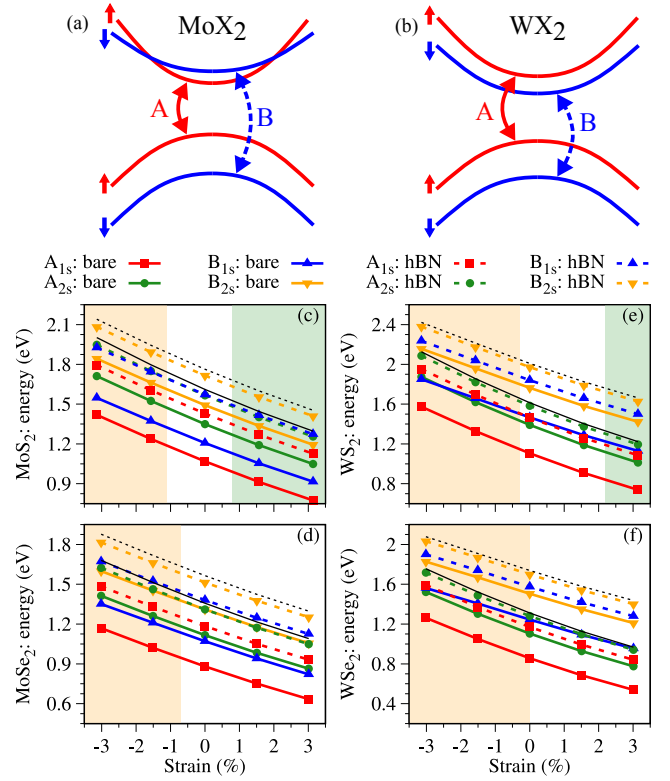


FIG. 6. (Color online) Sketch of the energy bands that contribute to the formation of A and B excitons in (a) Mo-based and (b) W-based TMDCs. Evolution of the total exciton energy as function of the biaxial strain for (c) MoS_2 , (d) MoSe_2 , (e) WS_2 and (f) WSe_2 . The thin solid (dashed) lines are the single-particle energies for the A (B) optical transitions. The shaded regions indicate indirect band gap regimes (K-Q for negative strain and Γ -K for positive strain).

citon peaks, i. e., the total energy given in Fig. 6(c-f), extracted as a linear fit in the -1.5% to 1.5% strain range. As a general trend, the strength of the gauge factors follow the order $\text{MoSe}_2 < \text{MoS}_2 < \text{WSe}_2 < \text{WS}_2$, and the effect of changing the dielectric surroundings modifies only 2 – 4 meV/%, which can be at the scale of experimental uncertainty. Although we have not taken into account corrections to the band gap, our calculated exciton behaviors are in good agreement with GW-BSE *ab-initio* calculations from Frisenda *et al.* [48], also shown in Table IV for comparison to our results. From the experimental perspective, the amount of studies on biaxial strain is still very scarce and mainly limited to MoS_2 . For the available gauge factors in MoS_2 , Plechinger *et al.* [42] found -105 meV/% for the A exciton, Lloyd *et al.* [45] -99 ± 6 meV/% for both A and B excitons and Gant *et al.* [49] a value of -94 meV/% for the A exciton. Furthermore, the study of Frisenda *et al.* [48] also determined experimentally the gauge factor of MoSe_2 , MoS_2 , WSe_2 and WS_2 but the values are smaller than the theoretical results, most likely because the strain present in the substrate is not fully transferred to the TMDC and

TABLE IV. Gauge factors (in meV/%) for single-particle transitions and exciton levels, extracted by linear extrapolation within the -1.5% to 1.5% strain range. The single-particle energies for the A and B optical transitions are presented as E_A and E_B .

| | MoS ₂ | MoSe ₂ | WS ₂ | WSe ₂ |
|-----------------|------------------|-------------------|-----------------|------------------|
| This work | | | | |
| E_A | -112.5 | -98.6 | -144.0 | -131.2 |
| E_B | -109.8 | -97.2 | -123.8 | -109.7 |
| A_{1s} : bare | -103.3 | -89.6 | -134.1 | -121.1 |
| A_{2s} : bare | -106.2 | -92.0 | -137.8 | -124.7 |
| B_{1s} : bare | -101.7 | -89.5 | -118.1 | -104.4 |
| B_{2s} : bare | -104.1 | -91.5 | -120.2 | -106.2 |
| A_{1s} : hBN | -106.9 | -92.7 | -138.6 | -125.5 |
| A_{2s} : hBN | -110.4 | -96.1 | -142.3 | -129.3 |
| B_{1s} : hBN | -104.8 | -92.0 | -120.6 | -106.5 |
| B_{2s} : hBN | -107.9 | -95.0 | -122.7 | -108.6 |
| GW-BSE[48] | | | | |
| E_A | -134 | -115 | -156 | -141 |
| A_{1s} : bare | -110 | -90 | -151 | -134 |
| B_{1s} : bare | -107 | -89 | -130 | -111 |

the calibration is not a straightforward task, as already discussed by the authors [48].

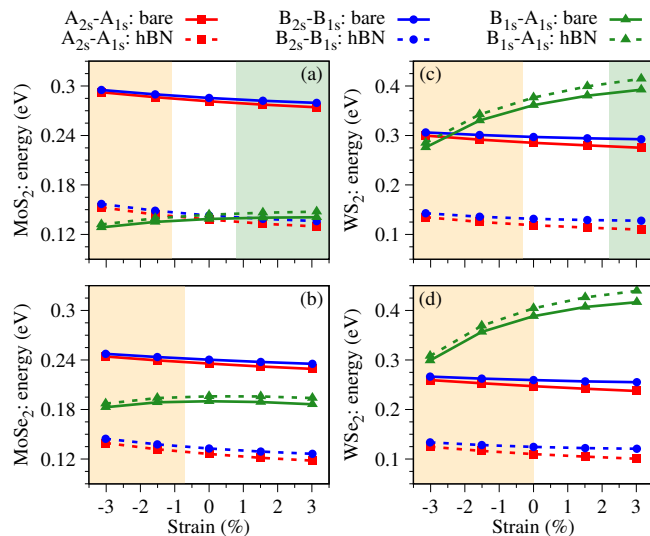


FIG. 7. (Color online) Evolution of the energy difference between distinct excitonic levels as function of the biaxial strain for (a) MoS₂, (b) MoSe₂, (c) WS₂ and (d) WSe₂. The shaded regions have the same meaning as in Fig. 6.

Besides the total exciton energies, it is also helpful to look at how the energy separation of different excitonic levels change under the applied strain. These behaviors are summarized in Fig. 7 for all TMDCs considered here and the corresponding gauge factors are presented in Table V. Although the change in the dielectric environment

TABLE V. Extracted gauge factors (in meV/%) for energy difference of single-particle transitions and excitonic levels.

| | MoS ₂ | MoSe ₂ | WS ₂ | WSe ₂ |
|------------------------|------------------|-------------------|-----------------|------------------|
| E_B-E_A | 2.7 | 1.4 | 20.2 | 21.5 |
| $A_{2s}-A_{1s}$: bare | -2.9 | -2.5 | -3.7 | -3.6 |
| $A_{2s}-A_{1s}$: hBN | -3.5 | -3.4 | -3.7 | -3.9 |
| $B_{2s}-B_{1s}$: bare | -2.5 | -2.0 | -2.1 | -1.8 |
| $B_{2s}-B_{1s}$: hBN | -3.1 | -2.9 | -2.1 | -2.1 |
| $B_{1s}-A_{1s}$: bare | 1.6 | 0.1 | 16.0 | 16.7 |
| $B_{1s}-A_{1s}$: hBN | 2.1 | 0.7 | 18.0 | 18.9 |

has a minor effect on the gauge factors (2 meV/% or less), it drastically changes the total energy difference by hundreds of meV for the $A_{2s}-A_{1s}$ and $B_{2s}-B_{1s}$ exciton separation (compare solid and dashed lines with squares and circles in Fig. 7). On the other hand the energy separation of $B_{1s}-A_{1s}$ excitons is affected by only a few or tens of meV (compare solid and dashed lines with triangles in Fig. 7). Furthermore, the gauge factor of $B_{1s}-A_{1s}$ energy difference for W-based compounds is one order of magnitude larger than that of the Mo-based compounds, reflecting the larger increase of λ_v (see for instance Fig. 4). We point out that for WSe₂ our calculations reveal the same qualitative trends as in recent experiments with uniaxial strain by Aslan *et al.* [46], in which they found a gauge factor of -6 ± 1 meV/% for the $A_{2s}-A_{1s}$ exciton separation and 10 meV/% for $B_{1s}-A_{1s}$ exciton separation.

V. SUMMARY

We have shown that applying biaxial strain to monolayer TMDCs induces drastic changes in their orbital, spin-orbit and, consequently, optical properties. Furthermore, we showed on a quantitative level, how the spin-orbit band splittings in a TMDC depend on biaxial strain and on the SOC contributions from the individual atoms. Additionally, by employing the Bethe-Salpeter equation combined with a minimal tight-binding Hamiltonian fitted to the *ab-initio* band structure, we have calculated the evolution of several direct exciton peaks as a function of biaxial strain and for different dielectric surroundings. Specifically, we found that the gauge factors are slightly affected by the dielectric environment and are mainly ruled by the atomic composition, with the ordering $\text{MoSe}_2 < \text{MoS}_2 < \text{WSe}_2 < \text{WS}_2$. Our results provide valuable insights into how strain can modify the TMDC properties within van der Waals heterostructures, and the parameter sets we provided can be applied to investigate other physical phenomena.

ACKNOWLEDGMENTS

We thank A. Polimeni for helpful discussions. This work was supported by DFG SPP 1666, DFG SFB 1277

(project B05), the European Unions Horizon 2020 research and innovation program under Grant No. 785219, the Alexander von Humboldt Foundation and Capes (Grant No. 99999.000420/2016-06).

-
- [1] A. Kormányos, G. Burkard, M. Gmitra, J. Fabian, V. Zólyomi, N. D. Drummond, and V. Fal'ko, *2D Materials* **2**, 022001 (2015).
- [2] G.-B. Liu, D. Xiao, Y. Yao, X. Xu, and W. Yao, *Chem. Soc. Rev.* **44**, 2643 (2015).
- [3] P. Tonndorf, R. Schmidt, P. Böttger, X. Zhang, J. Börner, A. Liebig, M. Albrecht, C. Kloc, O. Gordan, D. R. T. Zahn, S. Michaelis de Vasconcellos, and R. Bratschitsch, *Opt. Express* **21**, 4908 (2013).
- [4] S. Tongay, J. Zhou, C. Ataca, K. Lo, T. S. Matthews, J. Li, J. C. Grossman, and J. Wu, *Nano Lett.* **12**, 5576 (2012).
- [5] G. Eda, H. Yamaguchi, D. Voiry, T. Fujita, M. Chen, and M. Chhowalla, *Nano Lett.* **11**, 5111 (2011).
- [6] X. Li and J. Yang, *J. Mater. Chem. C* **2**, 7071 (2014).
- [7] V. Carreaux, D. Brunet, G. Ouvrard, and G. Andre, *J. Phys.: Condens. Mat.* **7**, 69 (1995).
- [8] C. Gong, L. Li, Z. Li, H. Ji, A. Stern, Y. Xia, T. Cao, W. Bao, C. Wang, Y. Wang, Z. Q. Qiu, R. J. Cava, S. G. Louie, J. Xia, and X. Zhang, *Nature* **546**, 265 (2017).
- [9] B. Siberchicot, S. Jobic, V. Carreaux, P. Gressier, and G. Ouvrard, *J. Phys. Chem.* **100**, 5863 (1996).
- [10] G. T. Lin, H. L. Zhuang, X. Luo, B. J. Liu, F. C. Chen, J. Yan, Y. Sun, J. Zhou, W. J. Lu, P. Tong, Z. G. Sheng, Z. Qu, W. H. Song, X. B. Zhu, and Y. P. Sun, *Phys. Rev. B* **95**, 245212 (2017).
- [11] Z. Wang, T. Zhang, M. Ding, B. Dong, Y. Li, M. Chen, X. Li, J. Huang, H. Wang, X. Zhao, Y. Li, D. Li, C. Jia, L. Sun, H. Guo, Y. Ye, D. Sun, Y. Chen, T. Yang, J. Zhang, S. Ono, Z. Han, and Z. Zhang, *Nat. Nanotechnol.* **13**, 554 (2018).
- [12] J. Liu, Q. Sun, Y. Kawazoe, and P. Jena, *Phys. Chem. Chem. Phys.* **18**, 8777 (2016).
- [13] W.-B. Zhang, Q. Qu, P. Zhu, and C.-H. Lam, *J. Mater. Chem. C* **3**, 12457 (2015).
- [14] M. A. McGuire, H. Dixit, V. R. Cooper, and B. C. Sales, *Chemistry of Materials* **27**, 612 (2015).
- [15] L. Webster, L. Liang, and J. A. Yan, *Phys. Chem. Chem. Phys.* **20**, 23546 (2018).
- [16] B. Huang, G. Clark, E. Navarro-Moratalla, D. R. Klein, R. Cheng, K. L. Seyler, D. Zhong, E. Schmidgall, M. A. McGuire, D. H. Cobden, W. Yao, D. Xiao, P. Jarillo-Herrero, and X. Xu, *Nature* **546**, 270 (2017).
- [17] P. Jiang, L. Li, Z. Liao, Y. Zhao, and Z. Zhong, *Nano Letters* **18**, 3844 (2018).
- [18] D. Soriano, C. Cardoso, and J. Fernandez-Rossier, *Solid State Communications* **299**, 113662 (2019).
- [19] B. Huang, G. Clark, D. R. Klein, D. MacNeill, E. Navarro-Moratalla, K. L. Seyler, N. Wilson, M. A. McGuire, D. H. Cobden, D. Xiao, W. Yao, P. Jarillo-Herrero, and X. Xu, *Nature Nanotechnology* **13**, 544 (2018).
- [20] S. Jiang, L. Li, Z. Wang, K. F. Mak, and J. Shan, *Nat. Nanotechnol.* **13**, 549 (2018).
- [21] M. Wu, Z. Li, T. Cao, and S. G. Louie, *Nat. Commun.* **10**, 1 (2019).
- [22] M. Yoshida, J. Ye, T. Nishizaki, N. Kobayashi, and Y. Iwasa, *Appl. Phys. Lett.* **108**, 202602 (2016).
- [23] Y. Noat, J. A. Silva-Guillén, T. Cren, V. Cherkez, C. Brun, S. Pons, F. Debontridder, D. Roditchev, W. Sacks, L. Cario, P. Ordejón, A. García, and E. Canadell, *Phys. Rev. B* **92**, 134510 (2015).
- [24] X. Zhu, Y. Guo, H. Cheng, J. Dai, X. An, J. Zhao, K. Tian, S. Wei, X. Cheng Zeng, C. Wu, and Y. Xie, *Nat. Commun.* **7**, 11210 (2016).
- [25] S.-Y. Xu, Q. Ma, H. Shen, V. Fatemi, S. Wu, T.-R. Chang, G. Chang, A. M. M. Valdivia, C.-K. Chan, Q. D. Gibson, J. Zhou, Z. Liu, K. Watanabe, T. Taniguchi, H. Lin, R. J. Cava, L. Fu, N. Gedik, and P. Jarillo-Herrero, *Nature Physics* **14**, 900 (2018).
- [26] J. Fabian, A. Matos-Abiague, C. Ertler, P. Stano, and I. Žutić, *Acta Phys. Slov.* **57**, 342 (2007).
- [27] I. Žutić, J. Fabian, and S. Das Sarma, *Rev. Mod. Phys.* **76**, 323 (2004).
- [28] K. F. Mak, C. Lee, J. Hone, J. Shan, and T. F. Heinz, *Phys. Rev. Lett.* **105**, 136805 (2010).
- [29] A. Chernikov, T. C. Berkelbach, H. M. Hill, A. Rigosi, Y. Li, O. B. Aslan, D. R. Reichman, M. S. Hybertsen, and T. F. Heinz, *Phys. Rev. Lett.* **113**, 076802 (2014).
- [30] M. Gibertini, F. M. D. Pellegrino, N. Marzari, and M. Polini, *Phys. Rev. B* **90**, 245411 (2014).
- [31] G. Wang, A. Chernikov, M. M. Glazov, T. F. Heinz, X. Marie, T. Amand, and B. Urbaszek, *Rev. Mod. Phys.* **90**, 021001 (2018).
- [32] Q. H. Wang, K. Kalantar-Zadeh, A. Kis, J. N. Coleman, and M. S. Strano, *Nat. Nanotechnol.* **7**, 699 (2012), 1205.1822.
- [33] M. Gmitra and J. Fabian, *Phys. Rev. B* **92**, 155403 (2015).
- [34] Y. K. Luo, J. Xu, T. Zhu, G. Wu, E. J. McCormick, W. Zhan, M. R. Neupane, and R. K. Kawakami, *Nano Lett.* **17**, 3877 (2017).
- [35] A. Avsar, D. Unuchek, J. Liu, O. L. Sanchez, K. Watanabe, T. Taniguchi, B. Özyilmaz, and A. Kis, *ACS Nano* **11**, 11678 (2017).
- [36] J. R. Schaibley, H. Yu, G. Clark, P. Rivera, J. S. Ross, K. L. Seyler, W. Yao, and X. Xu, *Nature Reviews Materials* **1**, 16055 (2016).
- [37] F. Langer, C. P. Schmid, S. Schlauderer, M. Gmitra, J. Fabian, P. Nagler, C. Schüller, T. Korn, P. G. Hawkins, J. T. Steiner, U. Huttner, S. W. Koch, M. Kira, and R. Huber, *Nature* **557**, 76 (2018).
- [38] D. Zhong, K. L. Seyler, X. Linpeng, R. Cheng, N. Sivadas, B. Huang, E. Schmidgall, T. Taniguchi, K. Watanabe, M. A. McGuire, W. Yao, D. Xiao, K.-M. C. Fu, and X. Xu, *Science Advances* **3**, e1603113 (2017).
- [39] D. Xiao, G.-B. Liu, W. Feng, X. Xu, and W. Yao, *Phys. Rev. Lett.* **108**, 196802 (2012).

- [40] K. He, C. Poole, K. F. Mak, and J. Shan, *Nano Lett.* **13**, 2931 (2013).
- [41] H. J. Conley, B. Wang, J. I. Ziegler, R. F. Haglund, S. T. Pantelides, and K. I. Bolotin, *Nano Lett.* **13**, 3626 (2013).
- [42] G. Plechinger, A. Castellanos-Gomez, M. Buscema, H. S. van der Zant, G. A. Steele, A. Kuc, T. Heine, C. Schueller, and T. Korn, *2D Materials* **2**, 015006 (2015).
- [43] J. Ji, A. Zhang, T. Xia, P. Gao, Y. Jie, Q. Zhang, and Q. Zhang, *Chinese Phys. B* **25**, 077802 (2016).
- [44] R. Schmidt, I. Niehues, R. Schneider, M. Drüppel, T. Deilmann, M. Rohlfing, S. Vasconcellos, A. Castellanos-Gomez, and R. Bratschitsch, *2D Mater.* **3**, 21011 (2016).
- [45] D. Lloyd, X. Liu, J. W. Christopher, L. Cantley, A. Wadehra, B. L. Kim, B. B. Goldberg, A. K. Swan, and J. S. Bunch, *Nano Lett.* **16**, 5836 (2016).
- [46] O. B. Aslan, M. Deng, and T. F. Heinz, *Phys. Rev. B* **98**, 115308 (2018).
- [47] O. B. Aslan, I. M. Datye, M. J. Mleczko, K. Sze Cheung, S. Krylyuk, A. Bruma, I. Kalish, A. V. Davydov, E. Pop, and T. F. Heinz, *Nano Lett.* **18**, 2485 (2018).
- [48] R. Frisenda, M. Drüppel, R. Schmidt, S. Michaelis de Vasconcellos, D. Perez de Lara, R. Bratschitsch, M. Rohlfing, and A. Castellanos-Gomez, *npj 2D Mater. Appl.* **1**, 10 (2017).
- [49] P. Gant, P. Huang, D. P. de Lara, D. Guo, R. Frisenda, and A. Castellanos-Gomez, *Materials Today* **27**, 8 (2019).
- [50] D. Tedeschi, E. Blundo, M. Felici, G. Pettinari, B. Liu, T. Yildirim, E. Petroni, C. Zhang, Y. Zhu, S. Sennato, Y. Lu, and A. Polimeni, *Advanced Materials* **31**, 1903795 (2019).
- [51] O. Iff, D. Tedeschi, J. Martn-Snchez, M. Moczad-Dusanowska, S. Tongay, K. Yumigeta, J. Taboada-Gutierrez, M. Savaresi, A. Rastelli, P. Alonso-Gonzalez, S. Hfling, R. Trotta, and C. Schneider, *Nano Letters* **19**, 6931 (2019).
- [52] E. Blundo, M. Felici, T. Yildirim, G. Pettinari, D. Tedeschi, A. Miriametro, B. Liu, W. Ma, Y. Lu, and A. Polimeni, (2019), 1910.11847.
- [53] H. Peelaers and C. G. Van de Walle, *Phys. Rev. B* **86**, 241401 (2012).
- [54] P. Johari and V. B. Shenoy, *ACS Nano* **6**, 5449 (2012).
- [55] A. Castellanos-Gomez, R. Roldán, E. Cappelluti, M. Buscema, F. Guinea, H. S. van der Zant, and G. A. Steele, *Nano letters* **13**, 5361 (2013).
- [56] S. Kumar, A. Kaczmarczyk, and B. D. Gerardot, *Nano letters* **15**, 7567 (2015).
- [57] A. Branny, G. Wang, S. Kumar, C. Robert, B. Lassagne, X. Marie, B. D. Gerardot, and B. Urbaszek, *Applied Physics Letters* **108**, 142101 (2016).
- [58] N. V. Proscia, Z. Shotan, H. Jayakumar, P. Reddy, C. Cohen, M. Dollar, A. Alkaskas, M. Doherty, C. A. Meriles, and V. M. Menon, *Optica* **5**, 1128 (2018).
- [59] K. S. Novoselov, A. Mishchenko, A. Carvalho, and A. H. Castro Neto, *Science* **353**, aac9439 (2016).
- [60] A. K. Geim and I. V. Grigorieva, *Nature* **499**, 419 (2013), 1307.6718.
- [61] I. Žutić, A. Matos-Abiague, B. Scharf, H. Dery, and K. Belashchenko, *Materials Today* **22**, 85 (2019).
- [62] M. Gmitra, D. Kochan, P. Högl, and J. Fabian, *Phys. Rev. B* **93**, 155104 (2016).
- [63] K. Zollner, P. E. Faria Junior, and J. Fabian, *Phys. Rev. B* **100**, 085128 (2019).
- [64] K. Seyler, D. Zhong, B. Huang, X. Linpeng, N. P. Wilson, T. Taniguchi, K. Watanabe, W. Yao, D. Xiao, M. A. McGuire, K. M. Fu, and X. Xu, *Nano letters* **18**, 3823 (2018).
- [65] J. Qi, X. Li, Q. Niu, and J. Feng, *Physical Review B* **92**, 121403 (2015).
- [66] P. Hohenberg and W. Kohn, *Phys. Rev.* **136**, B864 (1964).
- [67] P. Giannozzi, S. Baroni, N. Bonini, M. Calandra, R. Car, C. Cavazzoni, D. Ceresoli, G. L. Chiarotti, M. Cococcioni, I. Dabo, A. D. Corso, S. Fabris, G. Fratesi, S. de Gironcoli, R. Gebauer, U. Gerstmann, C. Gougousis, A. Kokalj, M. Lazzeri, L. Martin-Samos, N. Marzari, F. Mauri, R. Mazzarello, S. Paolini, A. Pasquarello, L. Paulatto, C. Sbraccia, S. Scandolo, G. Sclauzero, A. P. Seitsonen, A. Smogunov, P. Umari, and R. M. Wentzcovitch, *J. Phys.: Condens. Mat.* **21**, 395502 (2009).
- [68] G. Kresse and D. Joubert, *Phys. Rev. B* **59**, 1758 (1999).
- [69] J. P. Perdew, K. Burke, and M. Ernzerhof, *Phys. Rev. Lett.* **77**, 3865 (1996).
- [70] N. Wakabayashi, H. G. Smith, and R. M. Nicklow, *Physical Review B* **12**, 659 (1975).
- [71] W. J. Schutte, J. L. De Boer, and F. Jellinek, *Journal of Solid State Chemistry* **70**, 207 (1987).
- [72] P. B. James and M. T. Lavik, *Acta Crystallographica* **16**, 1183 (1963).
- [73] A. Kormányos, V. Zólyomi, N. D. Drummond, and G. Burkard, *Phys. Rev. X* **4**, 011034 (2014).
- [74] K. Kośmider, J. W. González, and J. Fernández-Rossier, *Phys. Rev. B* **88**, 245436 (2013).
- [75] C.-H. Chang, X. Fan, S.-H. Lin, and J.-L. Kuo, *Phys. Rev. B* **88**, 195420 (2013).
- [76] L. Wang, A. Kutana, and B. I. Yakobson, *Annalen der Physik* **526**, L7 (2014).
- [77] D. Muoi, N. N. Hieu, H. T. Phung, H. V. Phuc, B. Amin, B. D. Hoi, N. V. Hieu, L. C. Nhan, C. V. Nguyen, and P. Le, *Chemical Physics* **519**, 69 (2019).
- [78] G. H. Ahn, M. Amani, H. Rasool, D.-h. Lien, J. P. Mastandrea, J. W. Ager III, M. Dubey, D. C. Chrzan, A. M. Minor, and A. Javey, *Nat. Commun.* **8**, 608 (2017).
- [79] E. Cappelluti, R. Roldán, J. A. Silva-Guillén, P. Ordejón, and F. Guinea, *Phys. Rev. B* **88**, 075409 (2013).
- [80] G.-B. Liu, W.-Y. Shan, Y. Yao, W. Yao, and D. Xiao, *Phys. Rev. B* **88**, 085433 (2013).
- [81] See Supplemental Material at [URL will be inserted by publisher] including Refs. [69, 86], where we show band structure animations, further fit results for WS₂, WSe₂, and MoSe₂ as function of the lattice constant, and a comparison between PBE and PBEsol functional for all TMDCs.
- [82] I. Niehues, R. Schmidt, M. Drüppel, P. Marauhn, D. Christiansen, M. Selig, G. Berghäuser, D. Wigger, R. Schneider, L. Braasch, R. Koch, A. Castellanos-Gomez, T. Kuhn, A. Knorr, E. Malic, M. Rohlfing, S. Michaelis de Vasconcellos, and R. Bratschitsch, *Nano Lett.* **18**, 1751 (2018).
- [83] M. Feierabend, A. Morlet, G. Berghäuser, and E. Malic, *Phys. Rev. B* **96**, 045425 (2017).
- [84] S. Aas and C. Bulutay, *Opt. Express* **26**, 28672 (2018).
- [85] S. Kunschuh, M. Gmitra, and J. Fabian, *Physical Review B* **82**, 245412 (2010).

- [86] J. P. Perdew, A. Ruzsinszky, G. I. Csonka, O. A. Vydrov, G. E. Scuseria, L. A. Constantin, X. Zhou, and K. Burke, *Phys. Rev. Lett.* **100**, 136406 (2008).
- [87] S. L. Chuang, *Physics of optoelectronic devices* (John Wiley, New York, 1995).
- [88] H. Haug and S. W. Koch, *Quantum Theory of the Optical and Electronic Properties of Semiconductors: Fifth Edition* (World Scientific Publishing Company, 2009).
- [89] D. Y. Qiu, F. H. da Jornada, and S. G. Louie, *Phys. Rev. Lett.* **111**, 216805 (2013).
- [90] M. Rohlfing and S. G. Louie, *Phys. Rev. B* **62**, 4927 (2000).
- [91] B. Scharf, G. Xu, A. Matos-Abiague, and I. Žutić, *Phys. Rev. Lett.* **119**, 127403 (2017).
- [92] B. Scharf, D. Van Tuan, I. Žutić, and H. Dery, *Journal of Physics: Condensed Matter* **31**, 203001 (2019).
- [93] D. Tedeschi, M. De Luca, P. E. Faria Junior, A. Granados del Águila, Q. Gao, H. H. Tan, B. Scharf, P. C. M. Christianen, C. Jagadish, J. Fabian, and A. Polimeni, *Phys. Rev. B* **99**, 161204 (2019).
- [94] P. E. Faria Junior, M. Kurpas, M. Gmitra, and J. Fabian, *Phys. Rev. B* **100**, 115203 (2019).
- [95] N. S. Rytova, *Moscow University Physics Bulletin* **3**, 18 (1967).
- [96] L. Keldysh, *Soviet Journal of Experimental and Theoretical Physics Letters* **29**, 658 (1979).
- [97] P. Cudazzo, I. V. Tokatly, and A. Rubio, *Phys. Rev. B* **84**, 085406 (2011).
- [98] T. C. Berkelbach, M. S. Hybertsen, and D. R. Reichman, *Phys. Rev. B* **88**, 045318 (2013).
- [99] A. V. Stier, N. P. Wilson, K. A. Velizhanin, J. Kono, X. Xu, and S. A. Crooker, *Phys. Rev. Lett.* **120**, 057405 (2018).

Supplemental Material: Strain-tunable orbital, spin-orbit, and optical properties of monolayer transition-metal dichalcogenides

Klaus Zollner,^{1,*} Paulo E. Faria Junior,¹ and Jaroslav Fabian¹

¹*Institute for Theoretical Physics, University of Regensburg, 93040 Regensburg, Germany*

In the Supplemental Material we show fit parameters for WS₂, MoSe₂, and WSe₂ as function of biaxial strain. Furthermore, we compare the results for MoS₂, WS₂, MoSe₂, and WSe₂ when using a different functional in the first-principles calculations.

S1. FITTING PARAMETERS FOR OTHER TMDCS

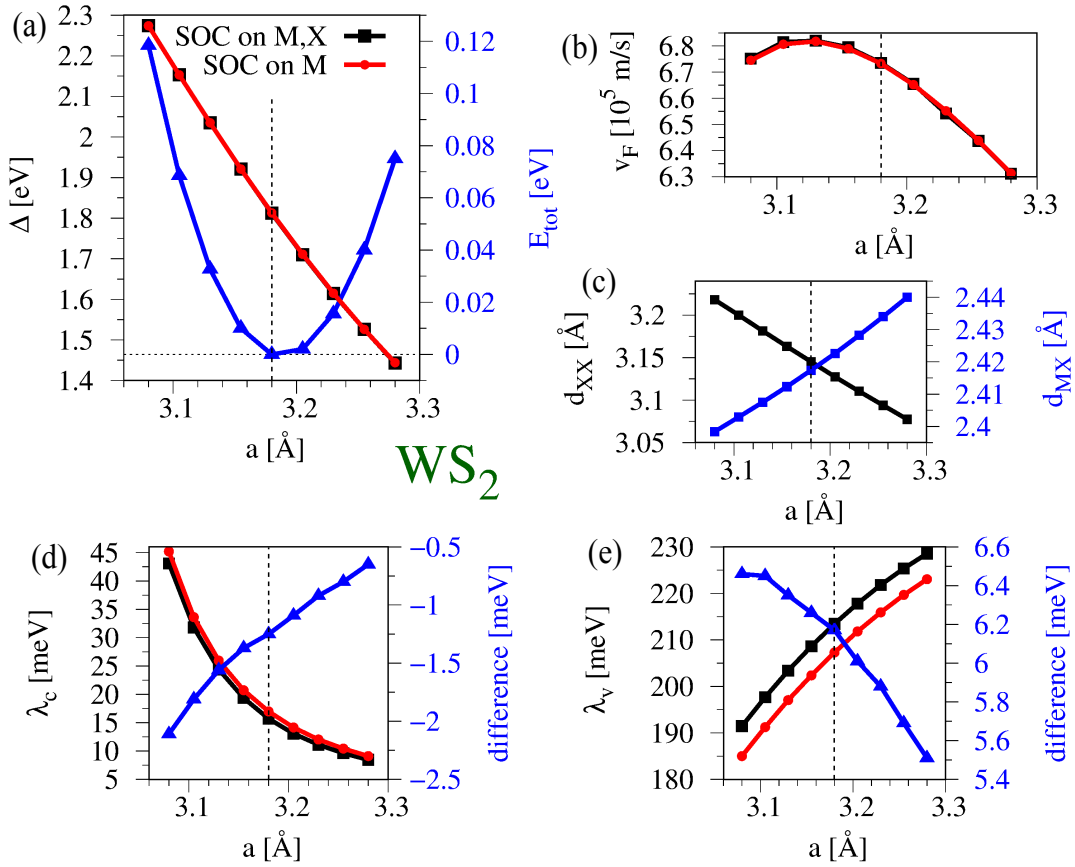


FIG. S1. (Color online) Summary of the fit parameters for WS₂ as a function of the lattice constant. (a) The gap parameter Δ and the total energy E_{tot} . The black data (SOC on M,X) correspond to calculations where SOC is included for both atoms M and X, while for the red data (SOC on M), we turned off SOC on the X atoms, respectively. Dashed vertical lines indicate the equilibrium lattice constant. (b) The Fermi velocity v_F . (c) The distances d_{XX} and d_{MX} . (d,e) The SOC parameters λ_c and λ_v . The difference (blue curve) is between the black and the red curve.

Similar to Fig. 4 of the main manuscript, we show the fit parameters for WS₂, MoSe₂, and WSe₂ in Figs. S1, S2, and S3. The observed dependence of the fit parameters, total energies, and distances on the lattice constant are similar to the case of MoS₂, shown in the main manuscript.

* klaus.zollner@physik.uni-regensburg.de

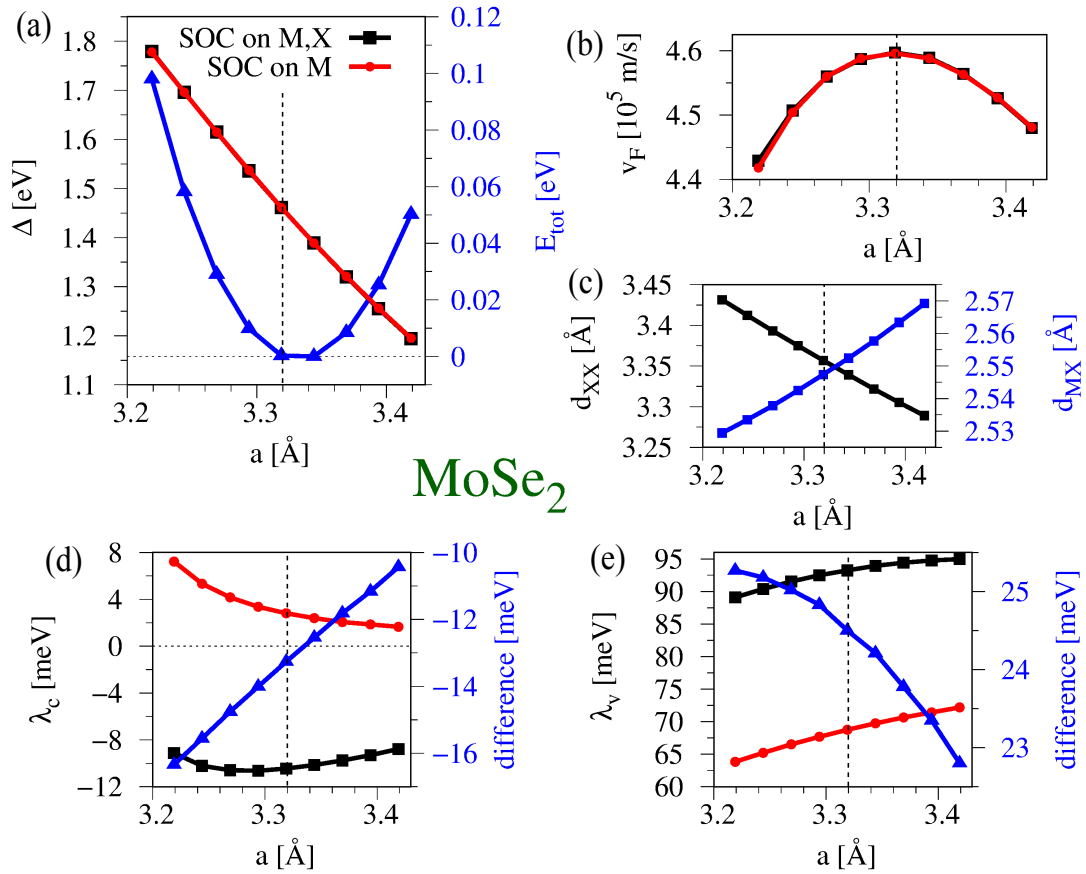


FIG. S2. (Color online) Same as Fig. S1, but for MoSe₂.

Comparing all four TMDC cases, we note that heavier elements (W, Se) give a larger contribution to spin-orbit band splittings than the lighter elements (Mo, S). For example, comparing Figs. S1(e) and S3(e), we find that the contribution from the Se atom to the VB SOC parameter is about 20 meV, while the one of the S atom is only about 6 meV.

S2. COMPARISON OF PBE AND PBESOL FUNCTIONAL

In Fig. S4, we compare the results from PBE [1] to the ones from PBEsol [2] exchange correlation functional, for the case of MoS₂. We find that the equilibrium lattice constant from PBEsol is $a = 3.15$ Å, in very good agreement with experiment, while PBE, giving $a = 3.185$ Å, overestimates the experimental lattice constant by about 1%. However, the trends that we observe for the fit parameters, as function of the lattice constant, are nearly the same for both functionals. Similarly, in Figs. S5, S6, and S7, we compare PBE and PBEsol functionals for MoSe₂, WS₂, and WSe₂. Again, the equilibrium lattice constant for PBEsol is in better agreement with the experimental value, but the general trends of all fit parameters are similar to the PBE functional.

We conclude that the PBEsol functional should hardly influence the results on exciton energy levels and gauge factors, and results can be compared to experiment, when regarding them relative to 0% strain (equilibrium lattice constant).

[1] J. P. Perdew, K. Burke, and M. Ernzerhof, Phys. Rev. Lett. **77**, 3865 (1996).

[2] J. P. Perdew, A. Ruzsinszky, G. I. Csonka, O. A. Vydrov, G. E. Scuseria, L. A. Constantin, X. Zhou, and K. Burke, Phys. Rev. Lett. **100**, 136406 (2008).

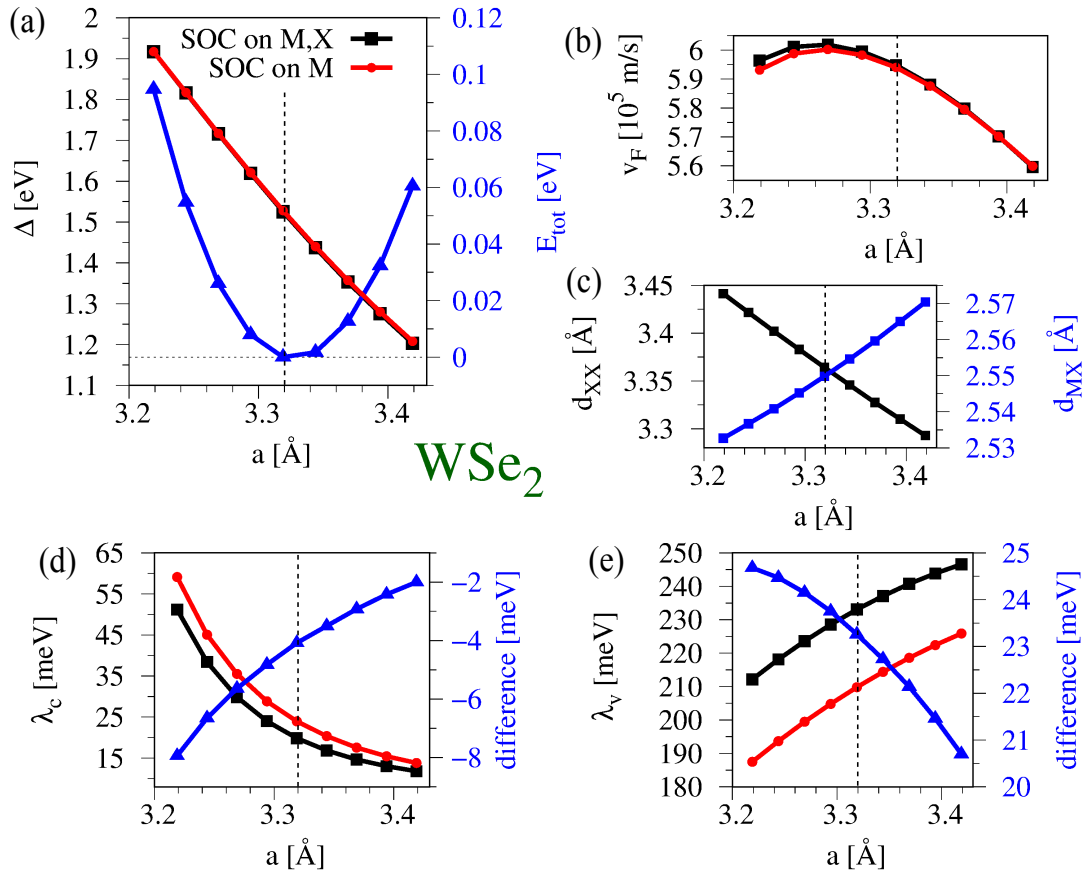


FIG. S3. (Color online) Same as Fig. S1, but for WSe_2 .

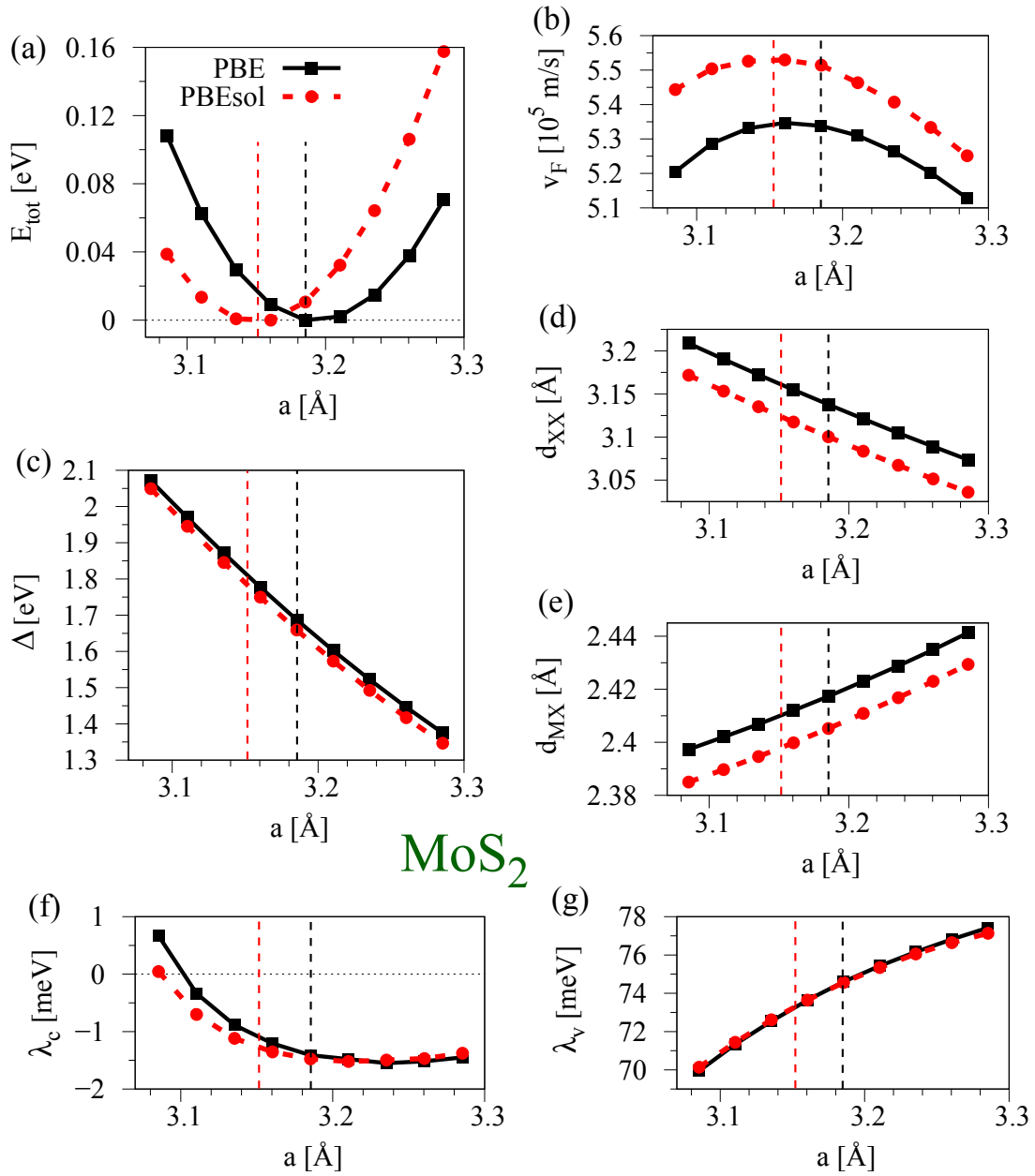


FIG. S4. (Color online) Comparison between the PBE (black squares) and PBEsol (red dots) functional for MoS₂ as function of the lattice constant. Dashed vertical lines indicate the equilibrium lattice constants. (a) Total energy E_{tot} , (b) the Fermi velocity v_F , (c) the gap parameter Δ , (d,e) the distances d_{XX} and d_{MX} , and (f,g) the SOC parameters λ_c and λ_v .

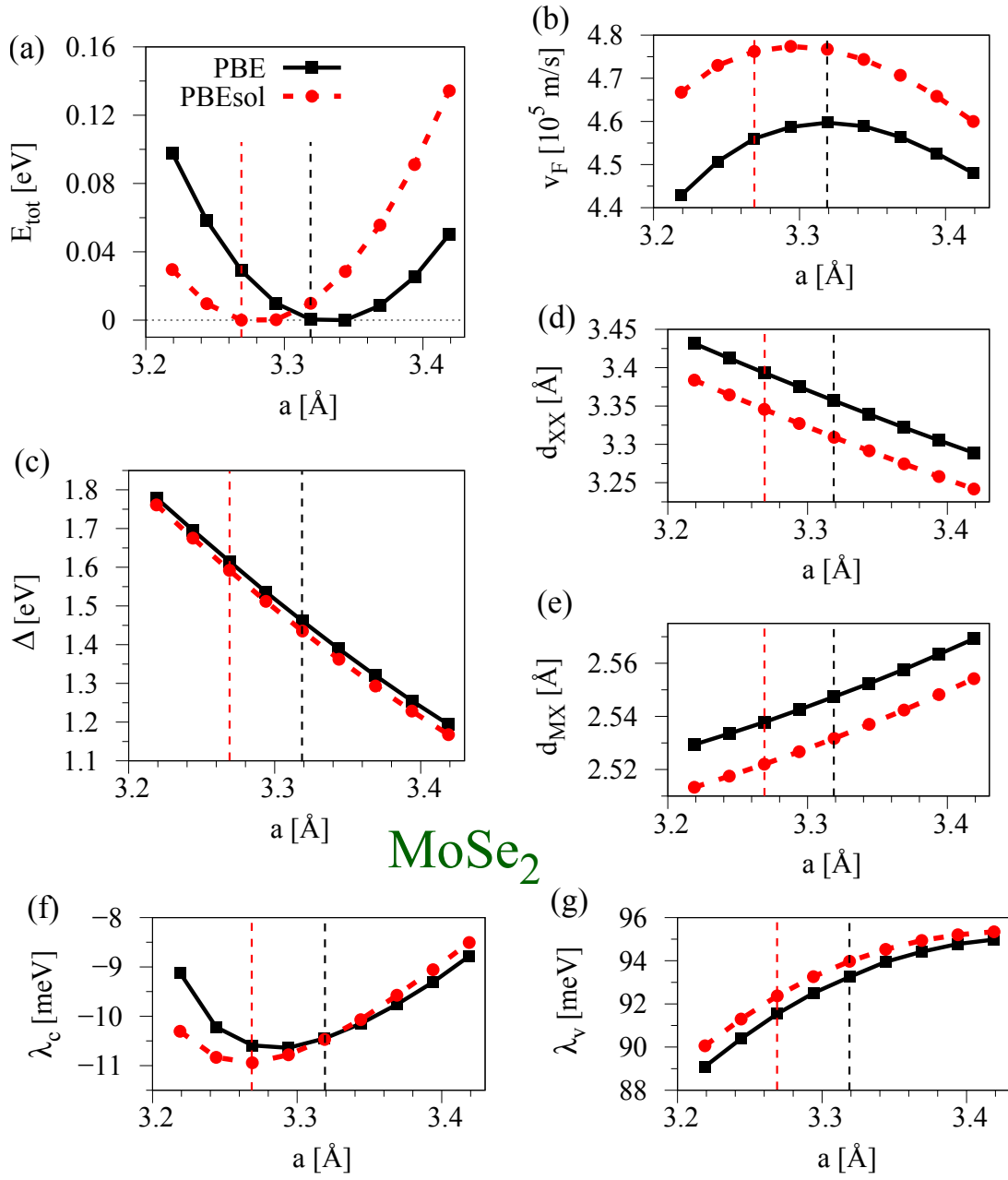


FIG. S5. (Color online) Same as Fig. S4, but for MoSe₂.

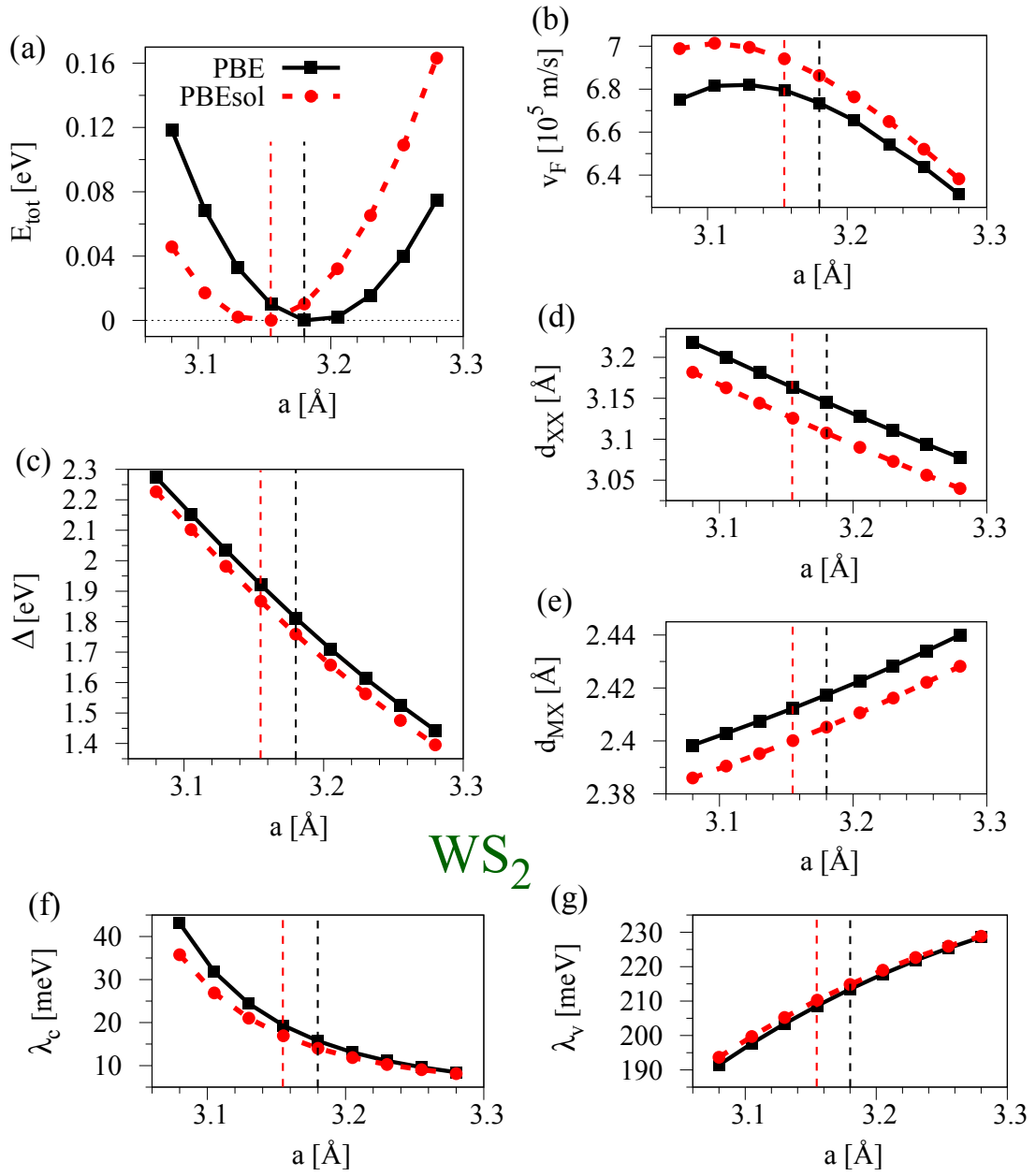


FIG. S6. (Color online) Same as Fig. S4, but for WS₂.

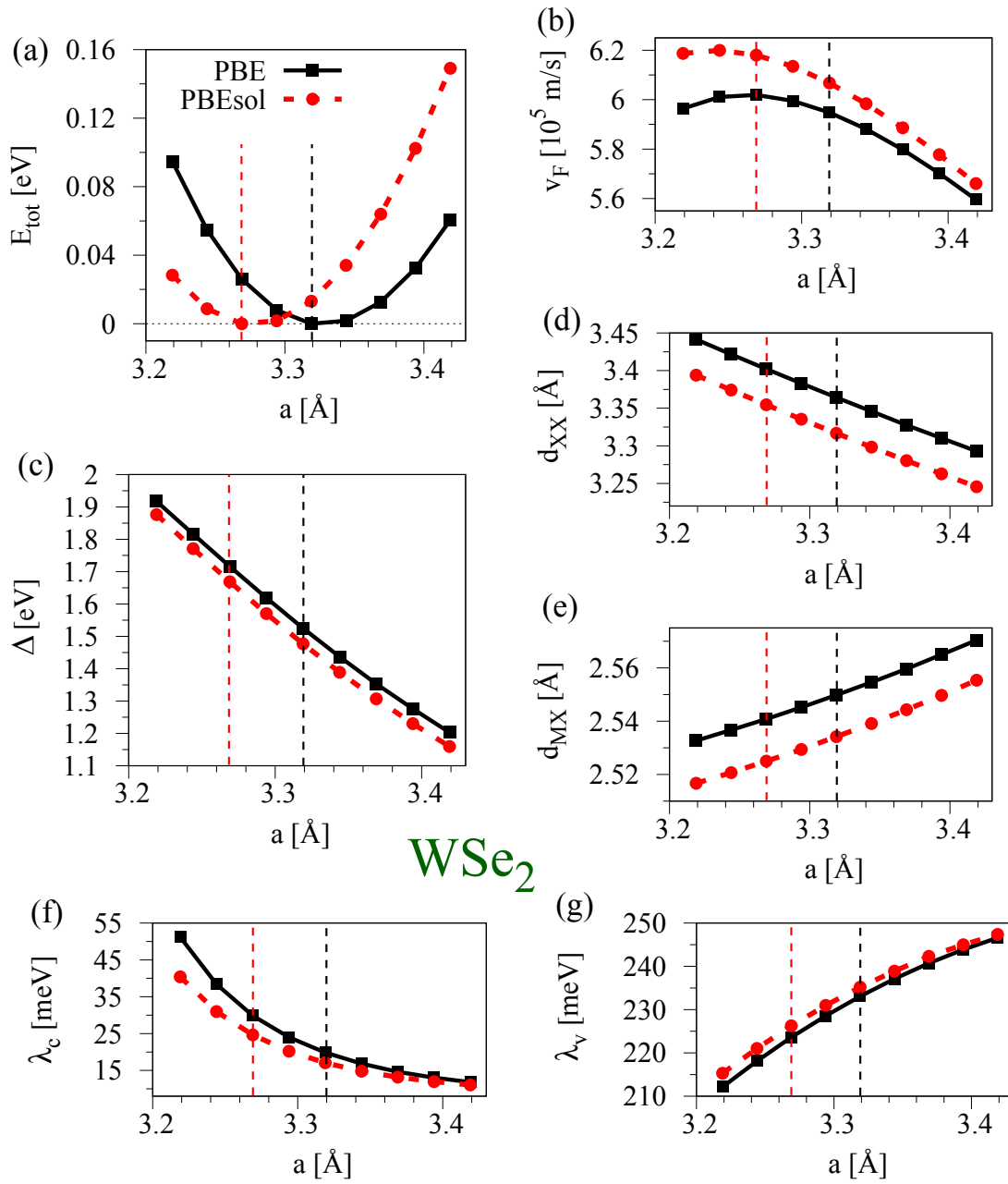


FIG. S7. (Color online) Same as Fig. S4, but for WSe₂.